



# A new strategy for capturing a noncooperative spacecraft by a robotic arm

Xiao-Yu Zhang<sup>1</sup> · Xiao-Feng Liu<sup>1</sup> · Ming-Ming Wang<sup>2</sup> · Guo-Ping Cai<sup>1</sup>

Received: 10 May 2022 / Accepted: 7 December 2022 / Published online: 30 December 2022  
© The Author(s), under exclusive licence to Springer Nature B.V. 2022

## Abstract

In robotic arm-based noncooperative spacecraft-capture missions, the gripper of the robotic arm collides with the target's surface and graspable structure. The former can cause the graspable structure to collide with the gripper multiple times or escape from the gripper. The adverse of the latter is that the momentum transfer can result in a sudden change in motion of the service spacecraft. If the service spacecraft is required to be in the desired configuration, the control system needs to generate a considerable control output. This paper designs a new capturing strategy to avoid these adverse phenomena, which divides the capture process into two phases: colliding and locking. In the colliding phase, the gripper will actively contact the target's surface and should maintain the contact, i.e., form a stable contact. This study proposes an improved damping-control scheme for forming a stable contact to realize this objective. Unlike the existing control scheme, this one allows the base of the service spacecraft to move, which helps to reduce the control force acting on the base, saving fuel. After establishing the stable contact, the gripper begins to close. The locking phase starts after forming a force-closure grasp. In this phase, the gripper will continue to close in a controlled manner. However, the states of the service spacecraft's base and robotic arm should transform from the controlled state to the uncontrolled state. A significant benefit is that the control system does not need to produce large control outputs to resist the colliding impact. Meanwhile, since the service spacecraft has a large inertia, the momentum transfer caused by the collision does not cause significant changes in its configuration. Numerical simulations are performed to evaluate the validity of the proposed control scheme and capturing strategy at the end of this paper. The results indicate that the proposals allow the space robot to grasp the target spacecraft with less control cost.

**Keywords** Noncooperative spacecraft · Robotic arm · Collision · Capture strategy · Improved damping-control scheme

---

✉ X.-F. Liu  
[peterliuxiaofeng@sjtu.edu.cn](mailto:peterliuxiaofeng@sjtu.edu.cn)

<sup>1</sup> State Key Laboratory of Ocean Engineering, Key Laboratory of Hydrodynamics of Ministry of Education, Shanghai Jiao Tong University, Shanghai 200240, China

<sup>2</sup> Science and Technology on Aerospace Flight Dynamics Laboratory, Northwestern Polytechnical University, Xi'an 710072, China

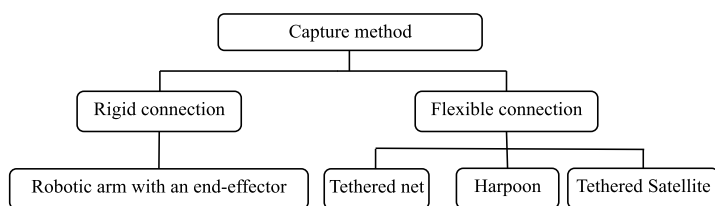


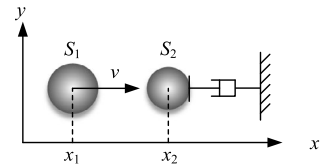
**Fig. 1** Capture methods

## 1 Introduction

The numbers of malfunctioning spacecraft are increasing rapidly with the increase of human space activities [1, 2]. This trend worsens the space-security situation and increases the tension on orbital resources. In order to eliminate the adverse effects caused by the increase of malfunctioning spacecraft, researchers have proposed two solutions: active removal and onorbit service. The industry and academia believe it is more reasonable to implement onorbit services for restorable high-value spacecraft. In this context, onorbit service has become a hot topic in the space field. Since the capturing operation is the first step of onorbit services, onorbit-capturing technology is critical among the various required technologies.

As a noncooperative target, most malfunctioning spacecraft do not require feature markers for measuring, a fixture for capturing, and active response devices for sending motion information. Furthermore, most of them are tumbling. These characteristics make the capture operation particularly challenging. Workers have proposed several capturing methods to successfully capture the failed spacecraft. As shown in Fig. 1, they can be divided into rigid and flexible connections. The rigid connection mainly employs a robotic arm with a rigid end-effector to capture the noncooperative target [3]. This method requires the target to have graspable structures such as a payload-attachment fitting (PAF) device or a rocket nozzle [4–6]. The flexible-connection capture method mainly adopts flying nets [7–13], harpoons [14–18], and flying claws [19, 20] as the capturing tools. These tools do not require that the target has graspable structures. Thus, more types of malfunctioning spacecraft can be captured using the flexible-connection method. However, since the research on this method started later than that on the rigid-connection method, this method has a disadvantage in technical maturity. Moreover, it is not easy to separate the capturing tools of flexible connection from the target. Thus, this method has a disadvantage in terms of reusability. In comparison, rigid connections are more beneficial in performing onorbit services of noncooperative spacecraft. Although the rigid connection has advantages in technical maturity and reusability, it is still a challenging and risky mission since the collision between the end-effector and the target can generate a significant impact. It can be said that any incorrect control will cause the failure of a capture mission and threaten the security of the service spacecraft. Therefore, the collision-control problem during capture deserves further study.

Various collision-control strategies have been proposed in the literature. For example, Yoshida et al. proposed the classical impedance-control-based methods [21–23]. Unlike the impedance-control method, Yoshida et al. introduced impedance matching into the designing process of the controller. The shortcoming of these methods is that the mass of the target and the contact parameters must be known. Similarly, Uyama et al. [24] proposed an impedance-based contact control of a free-flying space robot, employing the relative-motion information of the target to obtain the desired coefficient of restitution. Although the validity of this method was demonstrated through experiments, the target is a fixed wall and is not

**Fig. 2** Two-ball collision

free-floating. In order to apply this method for grasping the latter, Uyama et al. [25] added a compliant wrist on the end-effector and set compliant parameters equal to the contact ones in the following study. In this case, the compliant wrist was employed to acquire the relative-motion information of the target and the end-effector. Except for the mentioned modified impedance-control methods, Ma et al. [26], Flores-Abad et al. [27], Mou et al. [28], and Wu et al. [29] proposed different impedance-control methods. Although these methods have a better performance, they suffer from the same shortcoming as Yoshida's method. In order to overcome this shortcoming, a new collision-control method [30, 31] is proposed based on the damper ability to extend the two-balls collision's contact time, as shown in Fig. 2. Unlike the previous methods, the proposed method does not require the mass of the target and the contact parameter. In addition to active control methods, some researchers proposed compliance mechanisms to eliminate the adverse impacts of collision, such as the compliance wrist used by Stolfi et al. [32, 33] and the bioinspired antiimpact mechanism employed by Dai et al. [34].

The above literature review shows that although the existing studies have achieved good research results, they are not perfect and have some deficiencies. Moreover, most studies only consider one of the following collision cases: the end-effector colliding with the target's surface and the end-effector colliding with the target's graspable structure. However, both collisions will occur when employing grippers as the end-effector, and cause different adverse effects. The former can cause the graspable structure to collide with the gripper multiple times or escape from the gripper, namely cause the gripper to fail to close. The adverse of the latter is that the momentum transfer can result in a sudden change in motion of the service spacecraft. If the service spacecraft is required in a desired configuration, the control system needs to generate a considerable control output. It can be seen that ignoring any kind of collision is harmful to solve the capture-control problem. In this paper, the capture-control problem is split into a capture-strategy design problem and a collision-control problem. Aiming at the first problem, this paper designs a new capture strategy, which divides the capturing process into two phases: colliding and locking. In the colliding phase, the gripper will actively contact the target's surface and should maintain the contact, i.e., form a stable contact. After establishing the stable contact, the gripper begins to close. The locking phase starts after forming a force-closure grasp. In this phase, the gripper will continue to close until the graspable structure is locked. Since these two phases have different missions, their control objectives are different, and thus, their control schemes are different. The control objectives of the colliding phase are: 1) to form a stable contact between the gripper and the target's surface and 2) to form a force-closure grasp configuration. This study proposes an improved damping-control scheme, which can be regarded as an improved hybrid force/position control scheme. The control objectives of the locking phase are 1) to lock the graspable structure and 2) to reduce the control output. The employed scheme in this phase is that the gripper will continue to close in a controlled manner, but the service spacecraft's base and robotic arm should be transformed from a controlled state to a free one. Simulation results demonstrate the effectiveness of the proposed improved damping-control scheme and the capturing strategy. Compared with the existing studies, the main contributions of this paper mainly include the following aspects.

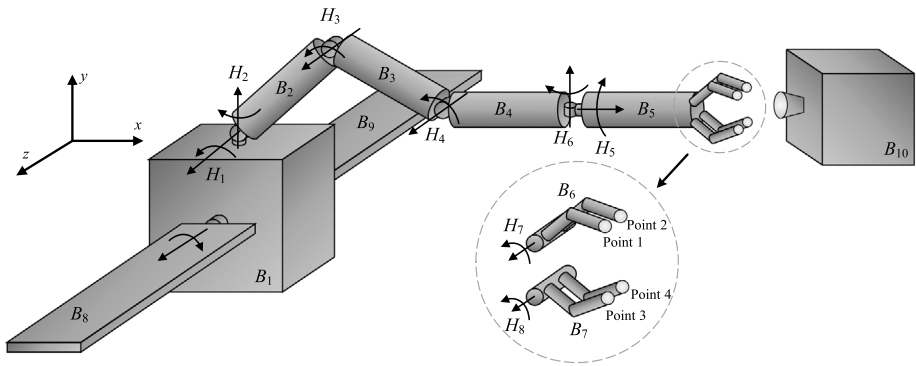


**Fig. 3** Space robot and noncooperative target

- (1) This study comprehensively analyzed the collision problem in the capture process and designed a new capture strategy. This strategy divides the capture process into colliding and locking phases according to the differences between collision scenarios, which helps solve the capture-control problem.
- (2) This study proposed an improved damping-control scheme to solve the control problem in the colliding phase, which can be regarded as a modified hybrid force/position control. Unlike the classical hybrid force/position control and the impedance-based control scheme, this scheme allows the base of the service spacecraft to move, reducing the control force acting on the base. From the viewpoint of energy, the new scheme can save fuel consumption during capture.

The rest of this paper is organized as follows. The dynamic model of the space robot and the contact model between the gripper and the target are presented in Sect. 2. Section 3 presents the design of the capturing strategy and the improved damping-control method. The numerical simulations are given in Sect. 4. Finally, Sect. 5 concludes the paper.

## 2 Dynamic models

In this section, the dynamic model of the space robot system is established. Then, the collision-contact-force model and the collision-detection algorithms are proposed in detail.

### 2.1 Dynamic model of the space robot

This paper takes a space robot as the service spacecraft to capture a noncooperative spacecraft, as presented in Fig. 3. The space robot comprises a rigid base (body  $B_1$ ), a rigid robotic arm (bodies  $B_2$ – $B_7$ ), and two flexible solar panels (bodies  $B_8$  and  $B_9$ ).  $H_i$  denotes the robotic arm's rotational joints. The noncooperative spacecraft is a rigid body with a nozzle cone. The nozzle cone is the captured structure, and the  $o$ -xyz frame is the inertial reference frame.

The dynamic equation of the robot can be expressed as [35]

$$-Z\dot{y} - z + h + f^{ey} = 0, \quad (1)$$

where  $y = [q_{base}^T, q_{arm}^T, q_{panel}^T]^T \in \mathbb{R}^{14+n}$  are the generalized coordinates, with  $q_{base} = [x, y, z, \alpha, \beta, \gamma]^T$  representing the position and attitude of the base,  $q_{arm} = [\phi_1, \phi_2, \dots, \phi_8]^T$

representing the joint angles of the robotic arm,  $\mathbf{q}_{panel} = [a_1, \dots, a_n]$  representing the modal coordinates of the panels vector;  $\mathbf{Z}$  is the generalized mass matrix;  $\mathbf{z}$  is the generalized inertia force relevant to  $\mathbf{y}$  and  $\dot{\mathbf{y}}$ ;  $\mathbf{h}$  is the generalized external force;  $\mathbf{f}^{ey} = [\mathbf{f}_{base}^T, \boldsymbol{\tau}_{arm}^T, \mathbf{0}_{1 \times n}]^T \in \Re^{(14+n) \times 1}$  is the generalized force, with  $\mathbf{f}_{base} \in \Re^{6 \times 1}$  representing the control force and control torque, and  $\boldsymbol{\tau}_{arm} \in \Re^{8 \times 1}$  representing the joint driving torques. Now, the dynamic model for this system is established; for details, please see Ref. [35].

## 2.2 Collision-contact force

Numerous contact-force models have been proposed [36–39]. They can be divided into two categories: linear models and nonlinear models. Since energy dissipation is considered in nonlinear models, they are more suitable for collision problems than linear ones. The Hertz-based Lankarani–Nikravesh (L–N) model is the most widely used nonlinear model in engineering [39, 40]. Hence, it is adopted in this paper to model the contact force, which can be expressed as [37, 40]

$$F_c = k_c d^n + \mu d^n \dot{d}, \quad (2)$$

where  $d$  is the penetration depth, and  $k_c$  is the contact stiffness, which depends on the material and contact surface curvature. The hysteretic damping coefficient  $\mu$  is defined as [36, 41]:

$$\mu = \frac{3k_c(1 - e^2)}{4\dot{d}^{(-)}}, \quad (3)$$

where  $\dot{d}^{(-)}$  is the value of  $\dot{d}$  at the beginning of the collision,  $e \in [0, 1]$  is the restitution coefficient,  $n$  depends on the topology characteristics of contact surfaces, which is set to be  $n = 1.5$  in this study.

## 3 Capture control

Since most noncooperative spacecraft do not have a customized graspable structure, the service spacecraft must choose some common structures to grasp. Rocket nozzles and payload-attachment fittings are geometrically similar to the custom structures allowing the gripper to form a force and geometric closure. Furthermore, they can withstand the capturing impact due to their high stiffness. Thus, rocket nozzles and payload-attachment fittings are relatively ideal graspable structures for noncooperative spacecraft. However, they have some shortcomings. The main one is that they are tightly connected to the target body surface, leaving no clearance at the connection. This shortcoming makes it difficult for the gripper to avoid colliding with the target's surface. This collision can produce two dynamic behaviors. The first results in the target moving away from the gripper, as shown in Fig. 4. The second results in a multitime collision, as shown in Fig. 5. Accordingly, the collision between the gripper and the target's surface is harmful to the capturing operation. This paper proposes an improved damping-control scheme to eliminate these two adverse effects. In addition to colliding with the target surface, the gripper must collide with the graspable structure during capturing. Similar to the first kind of collision, the second can also generate a large impact on the service spacecraft. Based on our simulation results, the control force and torque acting on the base when the gripper collides with the graspable structure are more significant than when the gripper collides with the target surface while using the improved damping-control

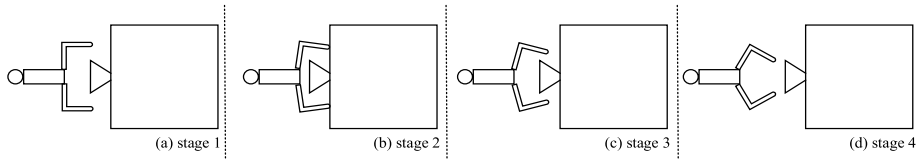


**Fig. 4** Separation

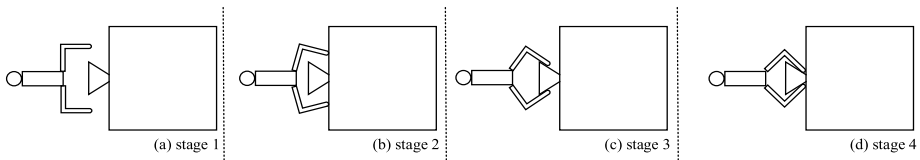


**Fig. 5** Multitimes collision

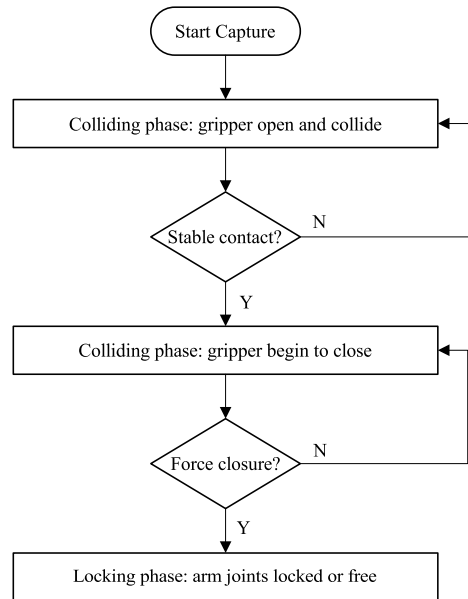
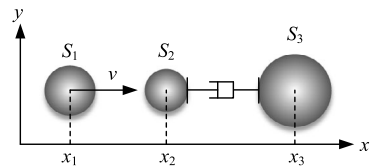
scheme to control the service spacecraft's motion. This indicates that different control strategies should be adopted before and after a collision with the graspable structure. Accordingly, this paper designs a new capture strategy to divide the capturing process into two phases: colliding and locking. The details of this strategy and the improved damping-control scheme are as follows.

### 3.1 Capture strategy

As introduced above, two collision scenarios exist between the gripper and the target spacecraft during capture. One is the collision with the target surface, and the other is the collision with the graspable structure. Considering they can cause different dynamic behaviors, employing different control schemes to reduce the adverse effects caused by them should be the best choice. Based on this ideal, this study designs a new capture strategy, which divides the capturing process into two phases according to the collision scenarios: colliding and locking. In the colliding phase, the gripper actively opens and collides with the target's surface. Once the collision occurs, the service spacecraft will control the motion of the base and the robotic arm to avoid the gripper moving away from the target surface, i.e., form a stable contact. In order to achieve this goal, an improved damping-control scheme is proposed, whose details will be given in Sect. 3.2. After establishing the stable contact, the gripper begins to close, forming the force-closure grasp. Once the force-closure grasp is formed, the operation enters the locking phase. In this phase, the gripper closes until the graspable structure is firmly grasped. To reduce the control output, the service-spacecraft's base and robotic arm need to be transformed from a controlled state to a free one during closing. The capturing flow diagram is depicted in Fig. 6.

### 3.2 Improved damping control

As introduced above, collision control plays a vital role in the proposed capturing strategy, which aims to avoid the separation of the gripper and the target's surface after a collision, i.e., to form a stable contact. Our previous work found that the damper can prevent the separation after collision by studying the system's dynamic behaviors, as shown in Fig. 2. Inspired by this, if the service-spacecraft's base, robotic arm, and gripper are, respectively,

**Fig. 6** Capturing flow diagram**Fig. 7** Three-ball collision system

regarded as the fixed end, damper, and ball  $S_2$ , and the captured target is regarded as the ball  $S_1$ , then the gripper motion can be controlled to avoid postcollision separation. A collision-control method named damping control was proposed and validated through simulations based on this idea. Based on the analysis results, constraining the base motion implies applying a considerable control force to the base to eliminate the collision impact. This is the major shortcoming of our previous control scheme, existing in other active methods, which will consume more fuel during capturing. This study modifies the system shown in Fig. 2 to the three-ball collision system in Fig. 7. By analyzing the dynamic behaviors of this system after the collision, it was found that the damper also can prevent postcollision separation. Accordingly, if the service-spacecraft's base, robotic arm, and gripper are regarded as the ball  $S_3$ , damper, and ball  $S_2$ , respectively, and the captured target is regarded as the ball  $S_1$ , then the motion of the base and the gripper can be controlled to avoid postcollision separation. This study proposes an improved damping-control scheme based on this idea. Since the scheme allows the base to move, the control force applied on it will be smaller. From the point view of energy, the new scheme can save fuel consumption during capture. In this subsection, the dynamic equations of the three-ball collision system are then constructed, and simulations are performed to illustrate the effect of the damper on the collision. Then, the design process of the improved control scheme is presented.

### 3.2.1 Effect of the damping on three-ball collision

Based on Newton's law and the L–N contact-force model and regardless of the radius, the dynamics equations of the three-ball collision can be expressed as:

$$\begin{cases} m_1 \ddot{x}_1 = -k_c(x_1 - x_2)^{1.5} - \frac{3k_c(1-e^2)}{4\dot{d}^{(-)}}(x_1 - x_2)^{1.5}(\dot{x}_1 - \dot{x}_2) \\ m_2 \ddot{x}_2 = k_c(x_1 - x_2)^{1.5} + \frac{3k_c(1-e^2)}{4\dot{d}^{(-)}}(x_1 - x_2)^{1.5}(\dot{x}_1 - \dot{x}_2) - c(\dot{x}_2 - \dot{x}_3) \\ m_3 \ddot{x}_3 = c(\dot{x}_2 - \dot{x}_3) \end{cases} \quad \text{if } x_1 - x_2 > 0$$

$$\begin{cases} m_1 \ddot{x}_1 = 0 \\ m_2 \ddot{x}_2 = -c(\dot{x}_2 - \dot{x}_3) \\ m_3 \ddot{x}_3 = c(\dot{x}_2 - \dot{x}_3) \end{cases} \quad \text{if } x_1 - x_2 \leq 0$$
(4)

where  $m_1$ ,  $m_2$ , and  $m_3$  are the masses of  $S_1$ ,  $S_2$ , and  $S_3$ , respectively,  $x_1$ ,  $x_2$ , and  $x_3$  are the  $x$ -coordinates of the three balls, and  $c$  is the damper's damping coefficient. When  $x_1 > x_2$ , the penetration depth is  $d = x_1 - x_2$ . In order to facilitate the subsequent derivation of the control method, let  $\alpha_1 = x_3 - x_1$  and  $\alpha_2 = x_2 - x_3$ , Eq. (4) can be rewritten as

$$\begin{cases} \ddot{x}_1 = -\frac{f_c}{m_1} \\ \ddot{\alpha}_1 = \frac{c\ddot{\alpha}_2}{m_3} + \frac{f_c}{m_1} \\ \ddot{\alpha}_2 = -\frac{(m_2 + m_3)}{m_2 m_3} c \ddot{\alpha}_2 + \frac{f_c}{m_2} \end{cases} \quad \text{if } \alpha_1 + \alpha_2 < 0$$

$$\begin{cases} \ddot{x}_1 = 0 \\ \ddot{\alpha}_1 = \frac{c\ddot{\alpha}_2}{m_3} \\ \ddot{\alpha}_2 = -\frac{(m_2 + m_3)}{m_2 m_3} c \ddot{\alpha}_2 \end{cases} \quad \text{if } \alpha_1 + \alpha_2 \geq 0$$
(5)

where  $f_c = k_c d^{1.5} \left(1 + \frac{3(1-e^2)}{4\dot{d}^{(-)}} \dot{d}\right)$  is the contact force,  $\alpha_1$  is the relative distance between  $S_3$  and  $S_1$ , and  $\alpha_2$  is the relative distance between  $S_3$  and  $S_2$ .

Now, several numerical simulations are performed to evaluate the influence of different damping coefficients on the collision results. Let the masses of  $S_1$ ,  $S_2$ , and  $S_3$  be  $m_1 = 100$  kg,  $m_2 = 10$  kg, and  $m_3 = 2000$  kg. The contact stiffness is  $k_c = 200\,000$ , and the restitution coefficient is  $e = 0.85$ . At the initial moment  $t = 0$ , the initial conditions are chosen as  $[x_1(0), x_2(0), x_3(0)] = [0, 0, 1 \text{ m}]$ , and  $[\dot{x}_1(0), \dot{x}_2(0), \dot{x}_3(0)] = [0.001 \text{ m/s}, 0, 0]$ . Figure 8 shows the simulation results when  $c = 0$  N s/m, 40 N s/m, 50 N s/m, 100 N s/m, 150 N s/m, and 200 N s/m, respectively. (Note that if the relative distance between  $S_1$  and  $S_2$  is positive,  $x_1 - x_2 > 0$ ,  $S_1$  contacts  $S_2$ .) As shown in Fig. 10, when damping  $c < 50$  N s/m, two balls  $S_1$  and  $S_2$  will immediately separate after they contact. When  $c = 50$  N s/m, the contact duration increases significantly with no separation between  $S_1$  and  $S_2$  in a long period. When  $c > 50$  N s/m, the contact duration will decrease with the increase of  $c$ . In spite of this, the contact duration of large damping is still far longer than that of no damping.



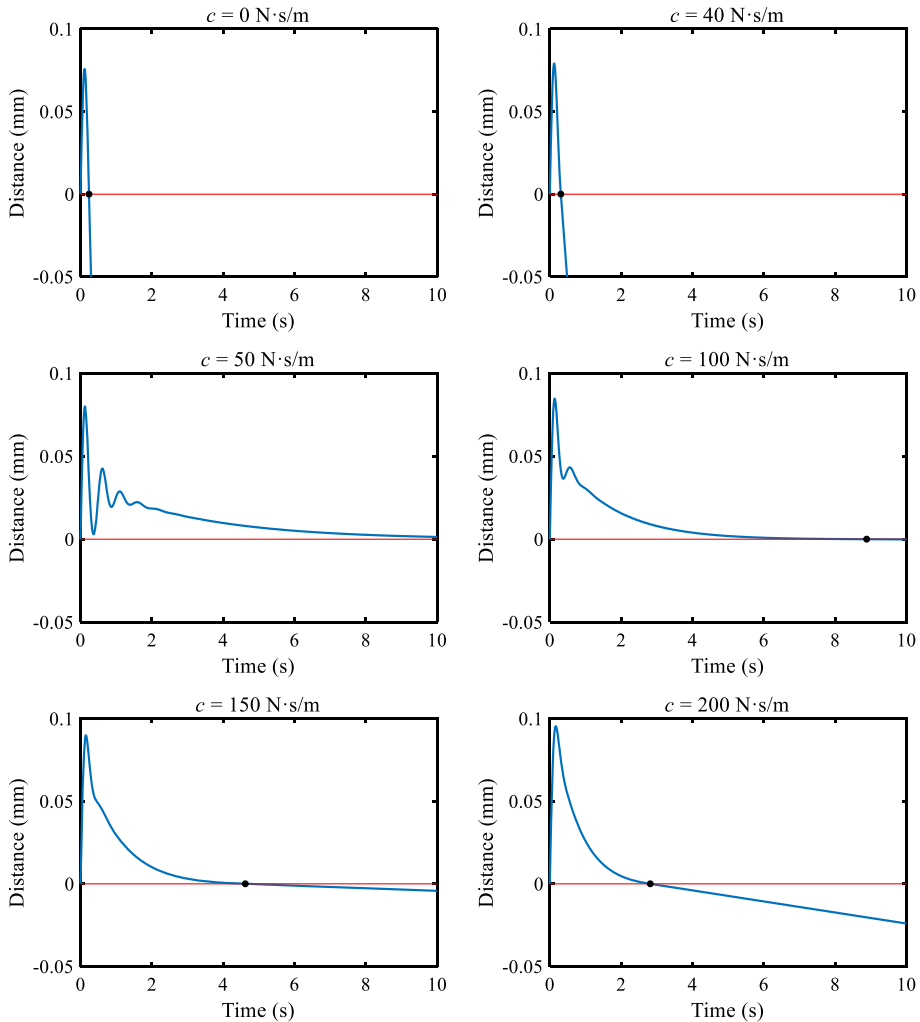
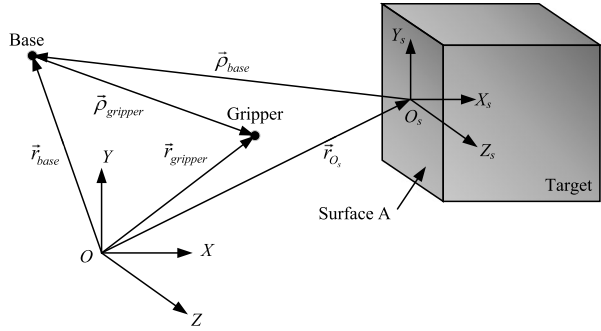


**Fig. 8** Relative distances between  $S_1$  and  $S_2$  for different damping coefficients

### 3.2.2 Improved damping scheme

The above simulation results demonstrate that the damper can extend the contact duration of the three-ball collision. Inspired by this finding, if the service-spacecraft's base, robotic arm, and gripper are regarded as ball  $S_3$ , damper, and ball  $S_2$ , respectively, and the captured target is regarded as the ball  $S_1$ , then the service-spacecraft motion can be controlled to avoid postcollision separation. This paper proposes an improved damping-control scheme based on this idea. This control scheme comprises a motion planner and a motion-tracking controller. The first function of the tracking controller is to maintain the relative attitude of the base and the gripper and the target's contact surface at zero during the collision. In this situation, the collision is similar to that shown in Fig. 7. The second function of the tracking controller is to make the base, the robotic arm, and the gripper move along the

Fig. 9 The frames on the target



desired trajectory generated by the motion planner. This paper employs the computed-torque method to design the tracking controller, whose detail can be found in [42]. The design idea of the motion planner comes from the collision system shown in Fig. 7. Next, this subsection will present the planner's details and the control system's block diagram.

As shown in Fig. 9, the inertial reference frame  $O$ - $XYZ$  is established on the target orbit. It only has a constant linear speed with respect to the geocentric frame, equal to the orbit speed. The  $O_s$ - $X_sY_sZ_s$  frame is a body-fixed frame on the contact surface  $A$ , whose origin  $O_s$  is on the cone's centerline.

Based on Eq. (5), the desired motion of the base and the desired relative motion between the base and the gripper along with the  $X_s$ -axis during the collision can be expressed as:

$$\begin{aligned}\ddot{x}_{base,s}^d &= \frac{C\dot{x}_{gripper-base,s}}{m_{base}} - \ddot{x}_{surface} \\ \ddot{x}_{gripper-base,s}^d &= -\frac{(m_{gripper}+m_{base})}{m_{gripper}m_{base}}C(\dot{x}_{gripper-base,s}) + \frac{f_c}{m_{gripper}},\end{aligned}\quad (6)$$

where  $m_{base}$  and  $m_{gripper}$  are the masses of the base and the gripper, respectively;  $C$  is the controlled damping,  $f_c$  is the normal contact force perpendicular to surface  $A$ ;  $\ddot{x}_{surface}$  is the projection of the acceleration of the surface on the  $X_s$ -axis;  $x_{base,s}^d$  is the relative position of the base on the  $X_s$ -axis, i.e., the first element of  $\mathbf{A}_{surface}^T(\mathbf{r}_{base} - \mathbf{r}_{O_s})$ ;  $x_{gripper-base,s}^d$  is the projection of the relative position between the base and the gripper on the  $X_s$ -axis, i.e., the first element of  $\mathbf{A}_{surface}^T(\mathbf{r}_{gripper} - \mathbf{r}_{base})$ ;  $\mathbf{A}_{surface}$  is the direction cosine matrix of  $O_s$ - $X_sY_sZ_s$  with respect to  $O$ - $XYZ$ , and  $\mathbf{r}_{O_s}$ ,  $\mathbf{r}_{gripper}$ , and  $\mathbf{r}_{base}$  are the position vectors of the point  $O_s$ , the gripper, and the base, respectively. The subscript  $s$  in Eq. (6) refers to the  $O_s$ - $X_sY_sZ_s$  frame.

By integrating Eq. (6),  $\dot{x}_{base,s}^d(t)$ ,  $x_{base,s}^d(t)$ ,  $\dot{x}_{gripper-base,s}^d(t)$ , and  $x_{gripper-base,s}^d(t)$  can be obtained. The base is expected to remain stationary on the  $Y_s$ - and  $Z_s$ -axes during the control, i.e.,  $\dot{y}_{base,s}^d(t) = y_{base,s}^d(t) = \dot{z}_{base,s}^d(t) = z_{base,s}^d(t) = 0$ . Meanwhile, the base and the gripper should have no relative motion on the  $Y_s$ - and  $Z_s$ -axes, i.e.,  $\dot{y}_{gripper-base,s}^d(t) = y_{gripper-base,s}^d(t) = \dot{z}_{gripper-base,s}^d(t) = z_{gripper-base,s}^d(t) = 0$ . When the position and velocity of  $O_s$  with respect to the  $O$ - $XYZ$  frame are known, those of the base and the gripper can be written as

$$\mathbf{r}_{base}^d(t) = \boldsymbol{\rho}_{base}(t) + \mathbf{r}_{O_s}(t) = \mathbf{A}_{surface}(t)\boldsymbol{\rho}'_{base}(t) + \mathbf{r}_{O_s}(t), \quad (7a)$$

$$\mathbf{r}_{gripper}^d(t) = \boldsymbol{\rho}_{gripper}(t) + \mathbf{r}_{base}(t) = \mathbf{A}_{surface}(t)\boldsymbol{\rho}'_{gripper}(t) + \mathbf{r}_{base}(t), \quad (7b)$$

where  $\boldsymbol{\rho}'_{gripper}(t) = [x_{gripper-base,s}^d(t), y_{gripper-base,s}^d(t), z_{gripper-base,s}^d(t)]^T$  and  $\boldsymbol{\rho}'_{base}(t) = [x_{base,s}^d(t), y_{base,s}^d(t), z_{base,s}^d(t)]^T$ .

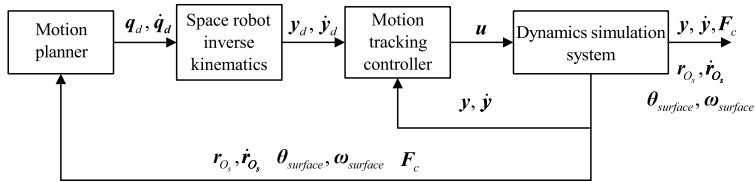


Fig. 10 Block diagram of the control system

Taking the time derivative of (7a), we have:

$$\dot{\mathbf{r}}_{base}^d(t) = \dot{\boldsymbol{\rho}}_{base} + \boldsymbol{\omega}_{surface}(t) \times \boldsymbol{\rho}_{base}(t) + \dot{\mathbf{r}}_{O_s}(t), \quad (8a)$$

$$\dot{\mathbf{r}}_{gripper}^d(t) = \dot{\boldsymbol{\rho}}_{gripper} + \boldsymbol{\omega}_{base}(t) \times \boldsymbol{\rho}_{gripper}(t) + \dot{\mathbf{r}}_{base}(t), \quad (8b)$$

where  $\dot{\boldsymbol{\rho}}_{base}(t) = \mathbf{A}_{surface}(t)[\dot{x}_{base,s}^d(t), \dot{y}_{base,s}^d(t), \dot{z}_{base,s}^d(t)]^T$ ,  $\dot{\boldsymbol{\rho}}_{gripper}(t) = \mathbf{A}_{base}(t)[\dot{x}_{gripper-base,s}^d(t), \dot{y}_{gripper-base,s}^d(t), \dot{z}_{gripper-base,s}^d(t)]^T$ .  $\boldsymbol{\omega}_{surface}(t)$  and  $\boldsymbol{\omega}_{base}(t)$  are the angular velocities of  $O_s$ - $X_s Y_s Z_s$  and the base with respect to  $O$ - $XYZ$ , respectively.  $\mathbf{A}_{base}$  is the direction cosine matrix of the base frame with respect to  $O$ - $XYZ$ .

The rotation of the base and the gripper should synchronize with that of the contact surface of the noncooperative target during the control, namely,

$$\boldsymbol{\theta}_{base}^d(t) = \boldsymbol{\theta}_{gripper}^d(t) = \boldsymbol{\theta}_{surface}(t), \quad \boldsymbol{\omega}_{base}^d(t) = \boldsymbol{\omega}_{gripper}^d(t) = \boldsymbol{\omega}_{surface}(t), \quad (9)$$

where  $\boldsymbol{\theta}_{base}^d$  and  $\boldsymbol{\theta}_{gripper}^d$  are the desired attitude angles of the base and the gripper, respectively,  $\boldsymbol{\omega}_{base}^d$  and  $\boldsymbol{\omega}_{gripper}^d$  are the desired angular velocities of the base and the gripper.  $\boldsymbol{\theta}_{surface}$  and  $\boldsymbol{\omega}_{surface}$  are the attitude angle and the angular velocity of the contact surface, which can be measured by lasers or cameras. Now, the desired configuration states  $\mathbf{y}_d(t)$  and  $\dot{\mathbf{y}}_d(t)$  can be easily obtained according to the inverse kinematics of the service spacecraft.

If the spacecraft tracks the desired motion, the collision between the service spacecraft and the target can be described by the system shown in Fig. 7. The separation between the colliding bodies can be prevented when the controlled damping is more significant than a specific critical value. In order to achieve this goal, the classic computed-torque method is employed for the motion-tracking controller, whose details can be found in [42]. The improved control scheme has been given; whose block diagram is depicted in Fig. 10.

## 4 Numerical simulations

This section evaluates the effectiveness of the improved damping-control method and compares its performance with the damping control proposed in Ref. [30]. The effectiveness of this capturing strategy will then be assessed.

### 4.1 Simulation settings

The structures of the space robot and the noncooperative target are shown in Fig. 3, in which the base ( $B_1$ ), the robotic arm ( $B_2$ – $B_5$ ), and gripper ( $B_6$ ,  $B_7$ ) of the service spacecraft and the target ( $B_8$ ) are rigid bodies, while their inertial parameters are presented in Table 1. The service-spacecraft's solar panels ( $B_9$ ,  $B_{10}$ ) are flexible bodies. Table 2 and Table 3 list the

**Table 1** Inertial parameters of the space robot and the noncooperative target

Body	Mass (kg)	$I_{xx}$ (kg m <sup>2</sup> )	$I_{yy}$ (kg m <sup>2</sup> )	$I_{zz}$ (kg m <sup>2</sup> )
$B_1$	2200	370	370	370
$B_2$	4	$6.5 \times 10^{-4}$	$5 \times 10^{-2}$	$5 \times 10^{-2}$
$B_3$	4	$6.5 \times 10^{-4}$	$5 \times 10^{-2}$	$5 \times 10^{-2}$
$B_4$	3.5	$4 \times 10^{-4}$	$3.5 \times 10^{-2}$	$3.5 \times 10^{-2}$
$B_5$	2.5	$3.5 \times 10^{-4}$	$3 \times 10^{-2}$	$3 \times 10^{-2}$
$B_6$	1.5	$1.5 \times 10^{-2}$	$9 \times 10^{-3}$	$9.3 \times 10^{-2}$
$B_7$	1.5	$1.5 \times 10^{-2}$	$9 \times 10^{-3}$	$9.3 \times 10^{-2}$
$B_8$	750	120	160	70

**Table 2** Inertial parameters of the solar panels ( $B_9$ ,  $B_{10}$ )

Parameters	Value
Length	2 m
Width	0.6 m
Thickness	0.02 m
Density	2700 kg/m <sup>3</sup>
Mass	64.8 kg
Modulus of elasticity	70 GPa
Poisson's ratio	0.3
Moment of inertia	diag (21.602, 1.946, 23.544) kg m <sup>2</sup>

parameters and the first five vibration modes of the panels. The lengths of the bodies  $B_2$ – $B_5$  are 0.6 m, 0.6 m, 0.4 m, and 0.2 m, respectively. The base  $B_1$  and the target  $B_8$  are cubes with sides of 1 m and 0.5 m. In all simulations, the restitution coefficient is  $e = 0.8$ . The initial position and attitude of the space robot and the target are shown in Fig. 11. The sample time of control is 3 ms. In addition, a first-order approximation model is used to describe the relation of the input and the output of the space robot's direct current (DC) torque motor, which are equipped in the robotic arm's joints. The expression of the approximation model is

$$\dot{T} = K_{gain}(T_d - T), \quad (10)$$

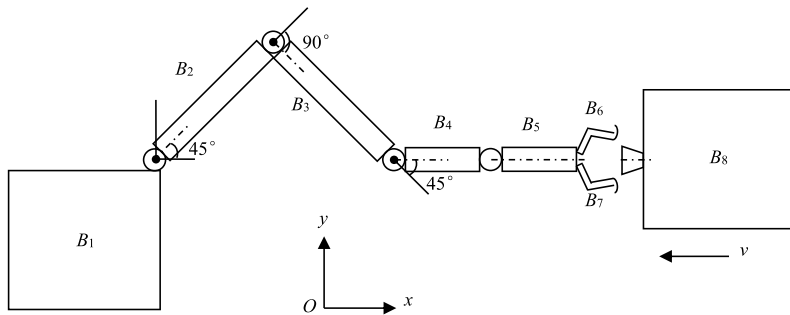
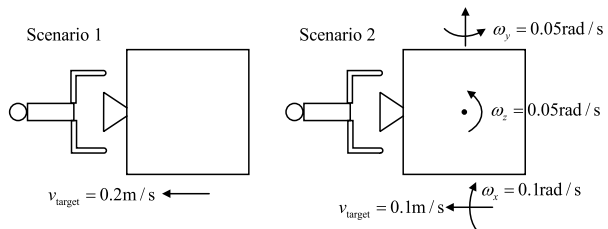
where  $T$  is the output torque,  $T_d$  is the desired output torque, and the gain coefficient  $K_{gain}$  is determined by the motor's electromagnetic time constant. Considering most advanced DC torque motors, such as the TMB+ series motors of ETEL Company, the electromagnetic time constant is about 8 ms. In this study, the electromagnetic time constant is set to be 8 ms. In order to simulate the dynamic characteristics,  $K_{gain}$  is set to 120.

## 4.2 Effectiveness of the improved control scheme

This subsection performs the simulations of two collision scenarios to evaluate the effectiveness of the proposed improved damping-control scheme and compare its performance with the original collision-control scheme [28, 29]. These two scenarios are presented in Fig. 12: (1) the target has only translational motion, whose linear velocity is  $[-0.2 \text{ m/s}, 0, 0]^T$ ; (2) the target has both translational and rotational motions, whose linear and angular velocities are

**Table 3** The first five vibration modes of the solar panels ( $B_9$ ,  $B_{10}$ )

Order	Mode	Frequency (Hz)
1st	1st-order bending mode	4.186
2nd	2nd-order bending mode	26.191
3rd	1st-order torsional mode	28.383
4th	3rd-order bending mode	73.718
5th	2nd-order torsional mode	88.577

**Fig. 11** Initial configurations of the space robot and noncooperative satellite**Fig. 12** Initial configurations of the two scenarios

$[-0.1 \text{ m/s}, 0, 0]^T$  and  $[0.1 \text{ rad/s}, 0.05 \text{ rad/s}, 0.05 \text{ rad/s}]^T$ , respectively. During simulations, the gripper stays open, and the controlled damping coefficient  $C$  is  $500 \text{ N s/m}$ . In these two scenarios, the contact stiffness is  $k_c = 1 \times 10^6$ .

During simulations, Fig. 13 and Fig. 14 depict the contact-penetration depths between the gripper and the target surface (Note: a positive penetration depth indicates there is contact, while a negative or zero one means there is no contact.) Figs. 15 and 16 show that the contact duration is very short when the service spacecraft is uncontrolled. In contrast, the contact duration is lengthened when the service spacecraft is under control, demonstrating that the original and improved control methods can prevent the separation of two collision bodies, i.e., both control methods effectively form a stable contact after the collision. Figure 15 and Fig. 16 depict the changes of the base's position and attitude. As shown in these two figures, when using the improved control scheme, the base can move. Observing the resultant control forces and torques acting on the base in Fig. 17 and Fig. 18, it can be seen that the improved scheme can reduce the control forces and torques. These phenomena indicate that allowing the base to move can reduce the control output. From an energy point of view, a larger control force means more power output from the engine. Considering the engine's power output is proportional to fuel consumption, a smaller control force means less fuel

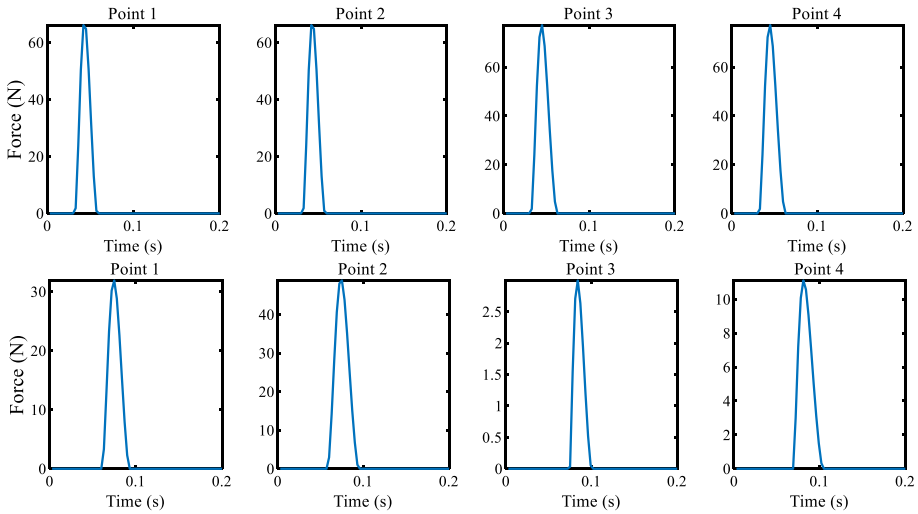


**Fig. 13** Contact forces between gripper points and the target surface without controller (the first and the second lines are the results in scenarios 1 and 2, respectively)

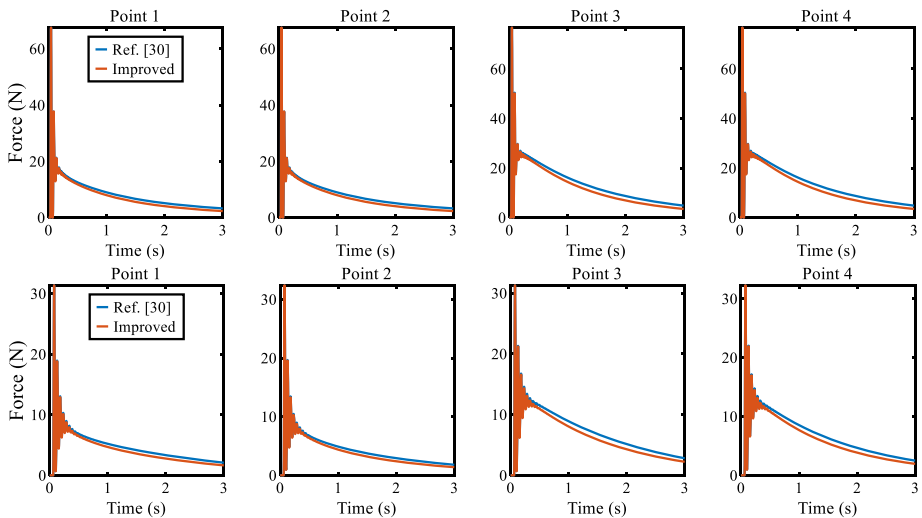


**Fig. 14** Contact forces between gripper points and the target surface with controllers (the first and the second lines are the results in scenarios 1 and 2, respectively)

consumption. Thus, the results in Fig. 17 and Fig. 18 demonstrate that the new scheme has the advantage of saving fuel. Figure 19 and Fig. 20 show that the improved scheme also can reduce the control torques acting on the arm joints, thus reducing the control effort. Figure 21 depicts the solar panel's vibration in the  $y$ -direction. Figure 22 depicts the vibration measuring point. As shown in Fig. 21, when using the original damping-control scheme, the vibration of the panels is on a small level because the base is not allowed to move during capturing. That is an advantage of the original damping-control scheme. However, this ad-

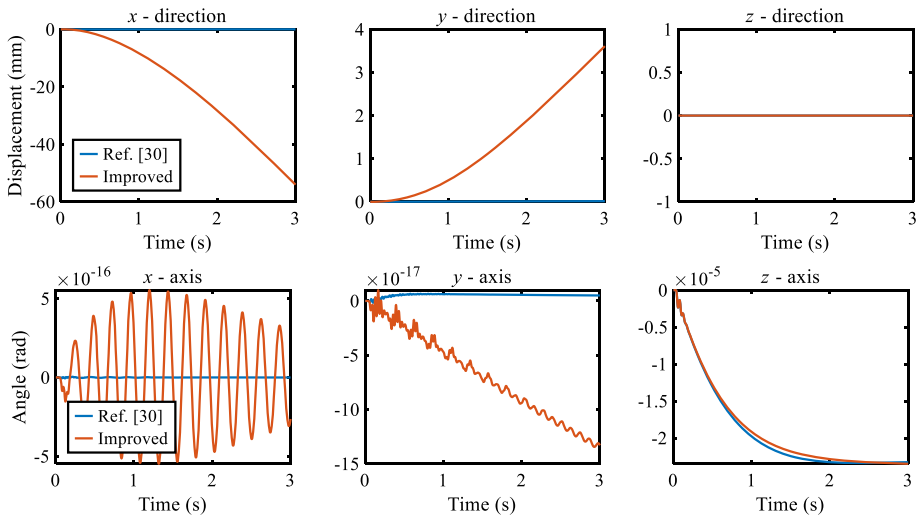


**Fig. 15** The changes of the base's position and attitude in scenario 1

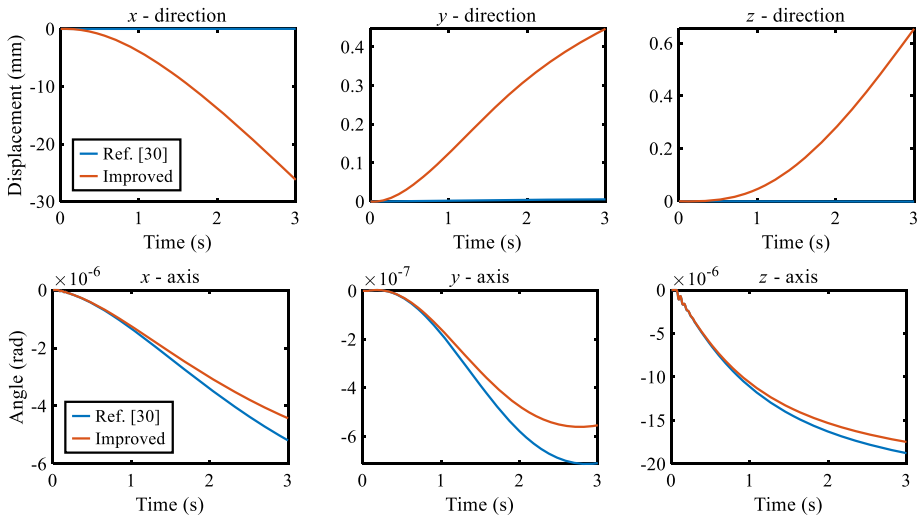


**Fig. 16** The changes of the base's position and attitude in scenario 2

vantage is not obvious since the vibration amplitude at the tip of the panels when using the improved control method is less than 0.01 mm. Considering the length of the panels is 2 m, the vibration can be ignored.

The above simulation results have verified the effectiveness of the proposed control method. Next, three new simulations were performed to evaluate the effect of different control-damping coefficients on the control result. The considered control damping coefficients are 500, 800, and 1000 N/s/m, respectively. Except for the controlled damping, the other simulation settings of these three simulations are the same as in scenario 1. All sim-

**Fig. 17** Resultant control forces and torques on the base in scenario 1

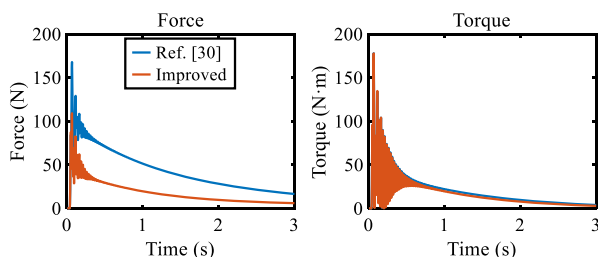


**Fig. 18** Resultant control forces and torques on the base in scenario 2

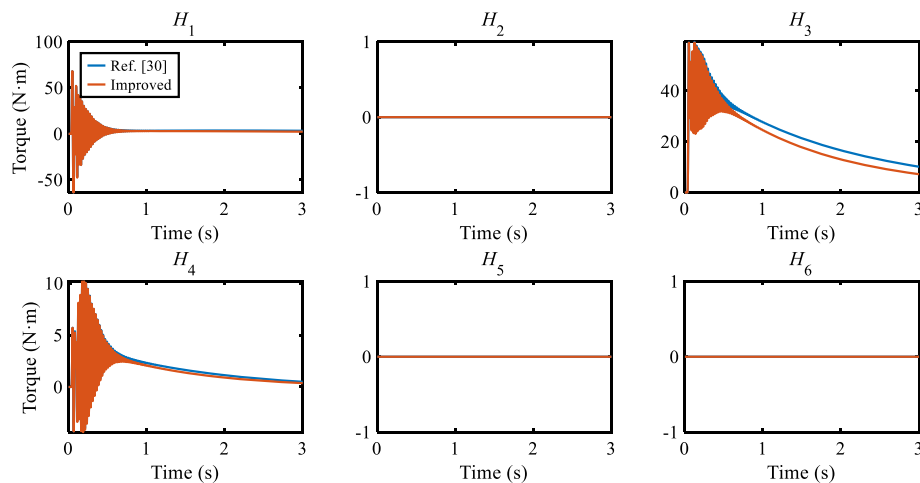
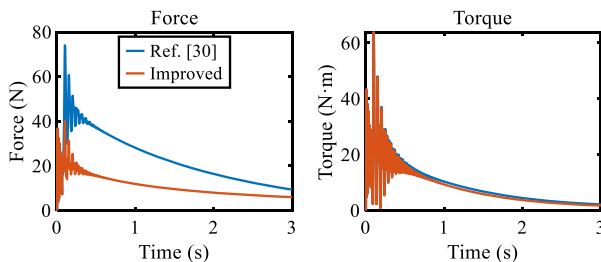


**Fig. 19** Control torques on arm joints in scenario 1

ulation results are shown in Figs. 23 to 27. As shown in Fig. 23, the penetration depth's descending speed is proportional to the controlled damping, indicating that greater damping will result in faster separation. Moreover, the maximum penetration depth is also proportional to the controlled damping. Figure 24 shows that the peak value of the resultant control force and torque increases with the increase of the controlled damping. Furthermore, the base's displacement and the solar panel's vibration in the  $y$ -direction increase with the increase of the controlled damping, as shown in Fig. 25 and Fig. 26. These simulation results indicate that the smaller control damping prolongs the contact duration and reduces the system's impact.



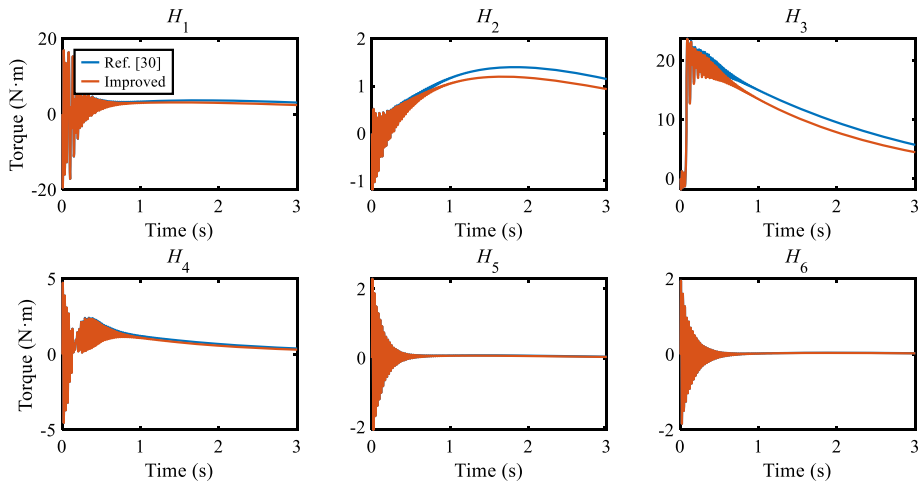


**Fig. 20** Control torques on arm joints in scenario 2

**Fig. 21** Vibration displacement of the endpoint of the solar panels in the  $y$ -direction with different scenarios

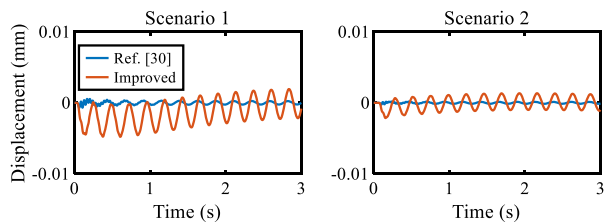
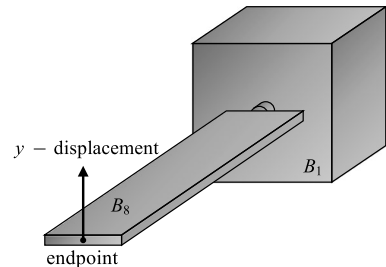


**Fig. 22** The endpoint of the solar panel



### 4.3 Robustness of the improved control strategy for uncertainty

In the capturing mission for noncooperative targets, the target's mass and the contact parameters are unknown before capture. Meanwhile, the measurement noise of the contact force is difficult to avoid. Whether the robustness of the proposed improved control scheme meets the requirement of the capturing mission is a problem worth studying. Here, four group simulations were carried out to test the robustness of the proposed control scheme.

The first group of simulations consider different inertia parameters of the target, which are listed in Table 4. The other settings are the same as those in the above scenario 1 and scenario 2. Figure 27 and Fig. 28 plot the simulation results. As shown in these figures, when the inertial parameters of the noncooperative target take different values, the proposed con-

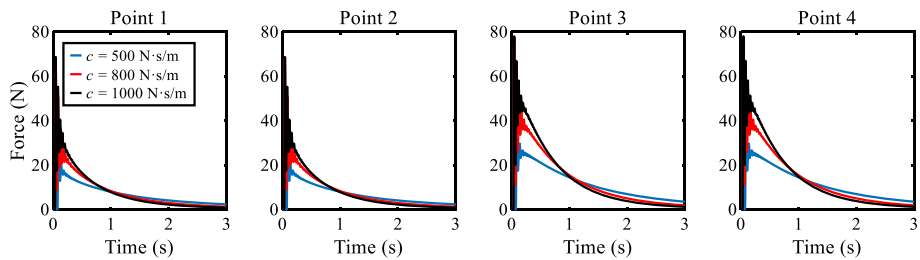


**Fig. 23** Contact forces between the gripper points and the target plane with different damping

**Fig. 24** Resultant control forces and torques on the base with different damping

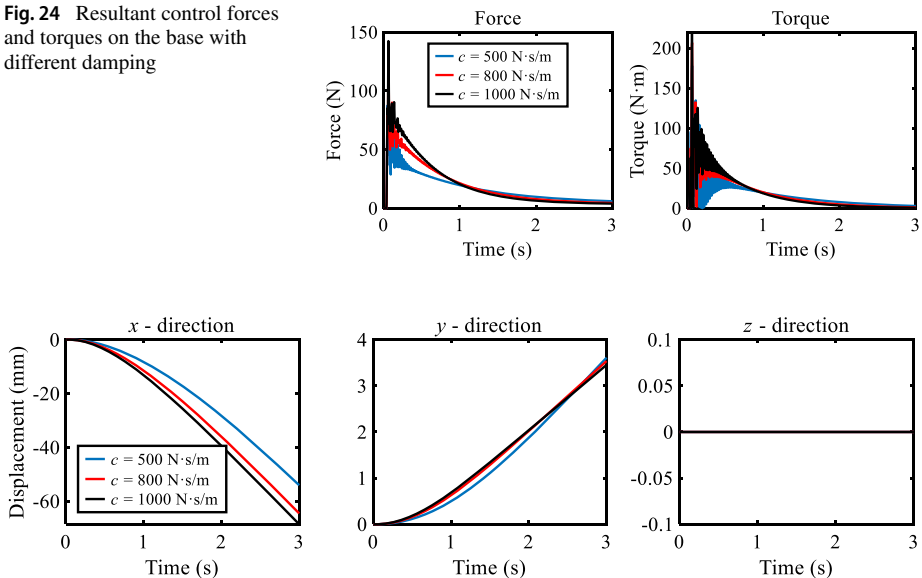


**Fig. 25** Displacement of the base with different damping

**Table 4** Inertial parameters of the noncooperative target

No.	Mass (kg)	$I_{xx}$ (kg m <sup>2</sup> )	$I_{yy}$ (kg m <sup>2</sup> )	$I_{zz}$ (kg m <sup>2</sup> )
Case 1	250	40	53.33	23.33
Case 2	500	80	106.67	46.67
Case 3 (default)	750	120	160	70
Case 4	1000	160	213.33	93.33
Case 5	1250	200	266.67	116.67

trol scheme can still achieve the objective without changing the control parameters, which demonstrates that the proposed scheme has robustness to the uncertainty of the target's inertia parameters.

The second group of simulations consider different contact stiffness, which are  $1 \times 10^4$ ,  $1 \times 10^5$ ,  $1 \times 10^6$ ,  $1 \times 10^7$ , and  $1 \times 10^8$ . The other settings are the same as those in the above

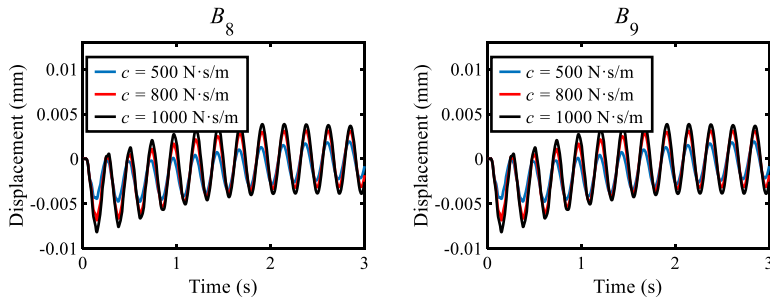


**Fig. 26** Vibration displacement of the endpoint of the solar panels in the  $y$ -direction with different damping

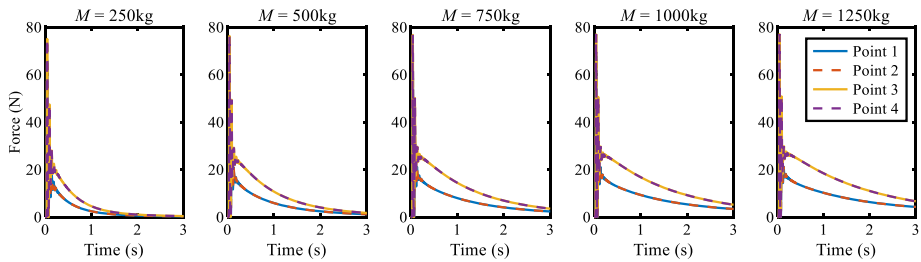


**Fig. 27** Contact forces between gripper points and the target plane with different inertia parameters of the target in scenario 1

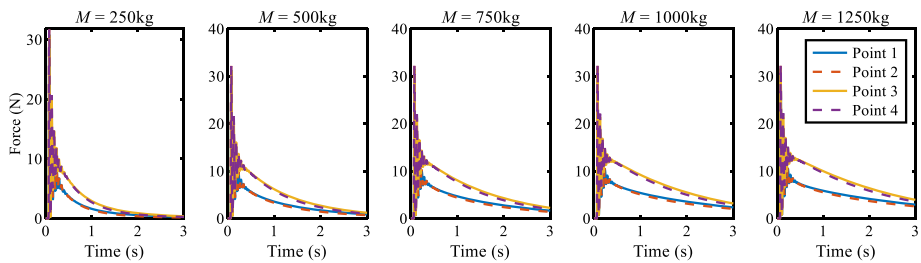


**Fig. 28** Contact forces between gripper points and the target plane with different inertia parameters of the target in scenario 2

scenario 1 and scenario 2. Figure 29 and Fig. 30 plot the simulation results. As shown in these figures, when the contact stiffness is smaller than  $1 \times 10^8$ , the contact force quickly enters a stable state, which illustrates that the separation between the gripper and the target is prevented. When the contact stiffness is  $1 \times 10^8$ , the contact force clearly oscillates, which illustrates that the gripper and the target frequently experience the “contact-separation” phenomenon. However, the gripper is not pushed away since the oscillation is at a high frequency. Although the frequency oscillation harms the space robot, the proposed control scheme can provide sufficient operation time for the closure of the gripper. Hence, the results in Fig. 29 and Fig. 30 demonstrate that the proposed scheme has robustness to the uncertainty of contact parameters without changing the control parameters.

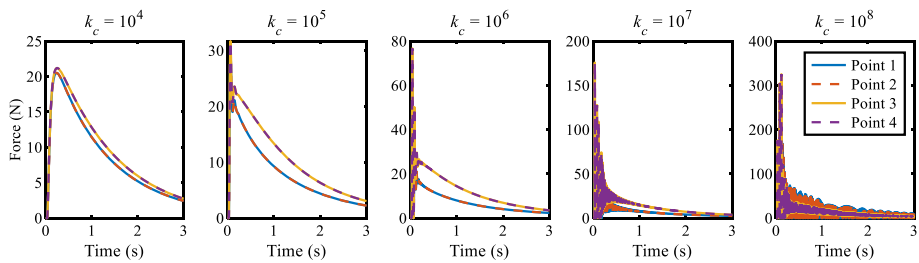


**Fig. 29** Contact forces between gripper points and the target plane with different stiffness in scenario 1

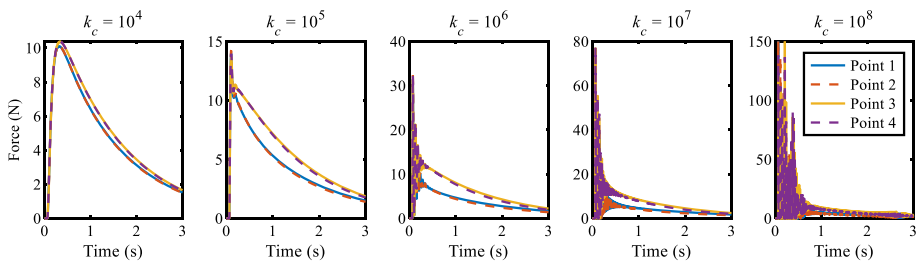


**Fig. 30** Contact forces between gripper points and the target plane with different stiffness in scenario 2

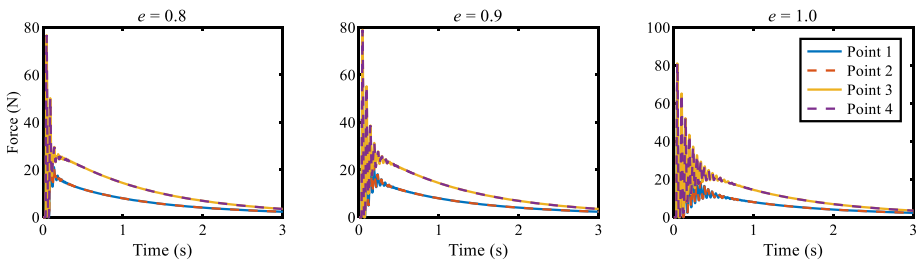


**Fig. 31** Contact forces between gripper points and the target plane with different coefficients of restitution in scenario 1

The third group of simulations consider different coefficients of restitution, which are 0.8, 0.9, and 1. The other settings are the same as those in the above scenario 1 and scenario 2. Figure 31 and Fig. 32 plot the simulation results. As shown in these figures, for the different coefficients of restitution, the proposed control scheme can still achieve the objective without changing the control parameters, which demonstrates that the proposed scheme has robustness to the uncertainty of contact parameters.

In the fourth group of simulations, three kinds of random noise are added to the measurement information of the contact force, whose amplitudes are 5%, 10%, and 15% of the measured value. Figure 33 and Fig. 34 plot the real contact force during simulation. These figures show that the contact force oscillates when there is noise in the measurement information, and the oscillations will be more obvious as the noise increases. Despite that, the noise does not disable the proposed control scheme. This illustrates that the proposed control scheme can resist the effects of noise. Considering that the noise can bring adverse

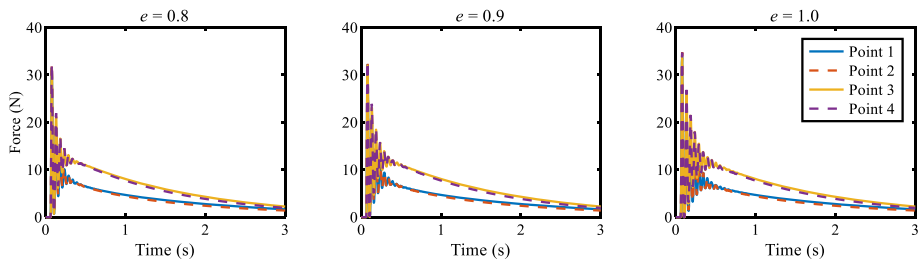


**Fig. 32** Contact forces between gripper points and the target plane with different coefficients of restitution in scenario 2

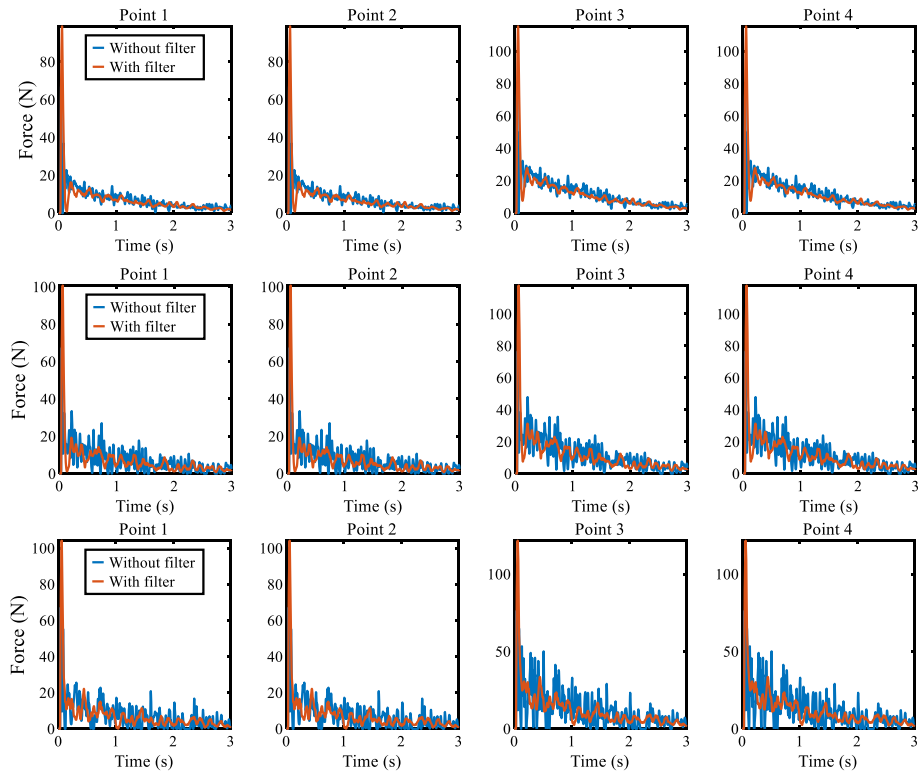


**Fig. 33** Real contact forces between gripper points and the target plane with different noise (5%, 10%, and 15% for each row, respectively) in scenario 1

effects on the capturing operation, this study adds a first-order Kalman filter to the control system to suppress them, whose expression is

$$X_k = \alpha Y_k + (1 - \alpha) X_{k-1}, \quad (11)$$

where  $X_k$  and  $X_{k-1}$  are the filtered results at  $k$  and  $k - 1$  moments, respectively,  $Y_k$  is the sampling result at  $k$  moment, and  $\alpha$  is the filter coefficient. In this study,  $\alpha$  is set to 0.25. As can be seen from Fig. 33 and Fig. 34, the Kalman filter is very effective in suppress-

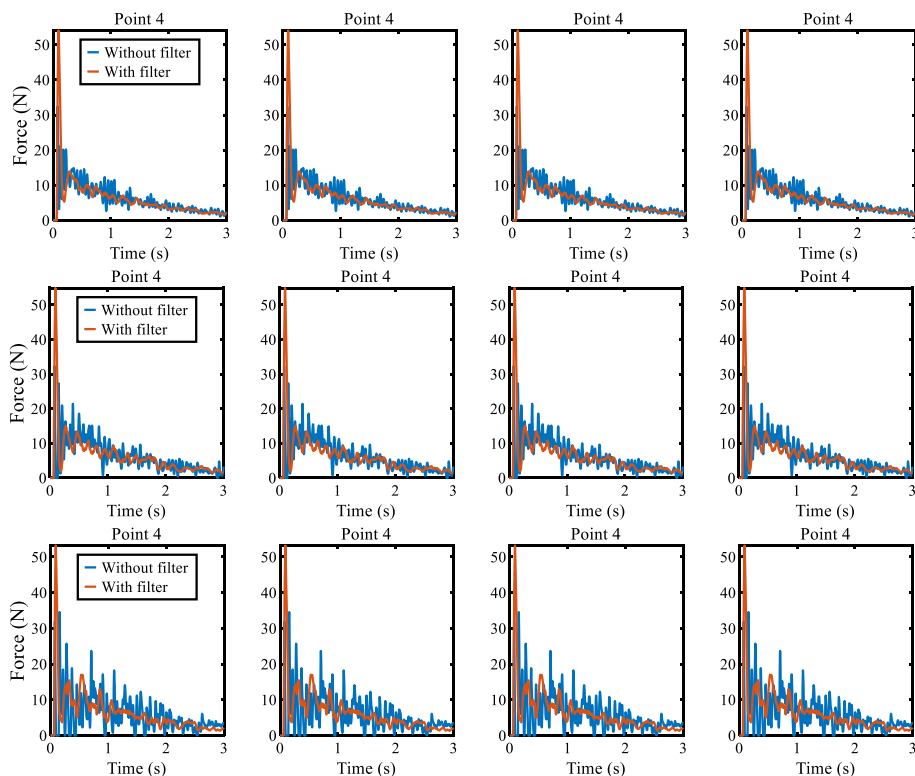


**Fig. 34** Real contact forces between gripper points and the target plane with different noise (5%, 10%, and 15% for each row, respectively) in scenario 2

ing contact oscillation. Furthermore, it can be seen that the Kalman filter can improve the robustness of the proposed control scheme for the measurement noise.

#### 4.4 Effectiveness of the capturing strategy

This subsection employs the three simulation scenarios shown in Fig. 35 to evaluate the effectiveness and advantage of the proposed strategy. In these simulations, a random noise is added to the measurement information of the contact force, whose amplitudes is 10% of the measured value. The other simulation settings are the same as those in Sect. 4.2. Figure 36 to Fig. 42 depict the simulation results of three capturing scenarios, where the legends “Improved” and “Free” refer to different control strategies used in the locking phase: “Improved” means the improved damping-control scheme controls the base and robotic arm; “Free” means the base and the robotic arm are both free. In the capturing process, the gripper begins to close at  $t = 3$  s. When the closing angle is less than 2.1 radians, the force-closure is formed, and then the capture enters the locking phase. As shown in Fig. 36 and Fig. 37, the capture enters the locking phase at about 4 s, while the gripper grasps the target at 4.5 s for both the controlled and uncontrolled states. It can be seen that the resultant control forces and torques of different simulation scenarios all increase rapidly at about 4.1 s when the improved damping-control scheme controls the service spacecraft in the locking phase. Moreover, the maximum of the locking phase is more significant than that of the collision

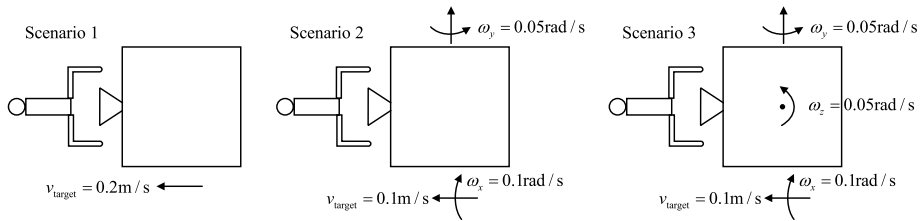


**Fig. 35** Initial configurations of the three scenarios

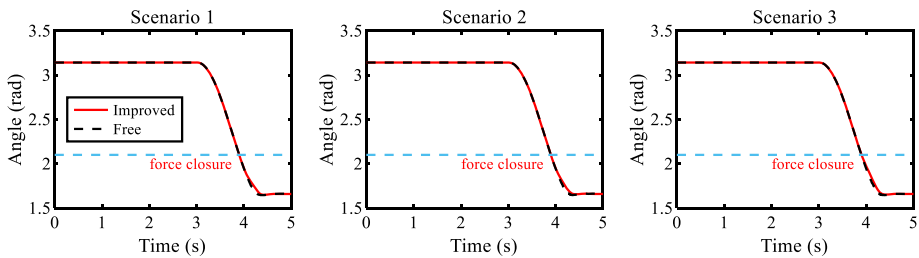


**Fig. 36** Closing angles of the gripper in different scenarios

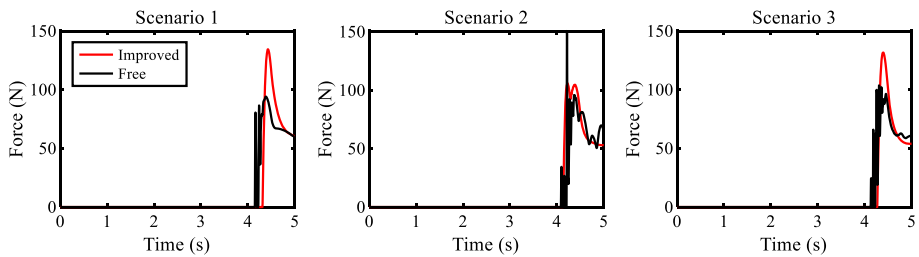


**Fig. 37** Contact forces between gripper's Point 1 and the nozzle cone in different scenarios

phase. This phenomenon occurs because the gripper will collide with the nozzle cone in the locking phase. After the collision occurs, the contact force will change the target's pose rapidly, varying the relative pose of the base and the target. Since the relative pose should be consistent with the desired one in the proposed collision-control scheme, it is necessary to apply a more significant control force and torque on the base to eliminate the contact's adverse effect. As shown in Fig. 38 and Fig. 39, the time point at which the control force and torque rise rapidly coincides with the collision time, demonstrating the correctness of the above analysis. Figure 40 plots the vibration of the panel. Observing this figure, we can see that when the base and the robotic arm are in the free state, the vibration of the panel will increase. Although the maximum vibration amplitude can reach about 0.2 mm, it is not significant, and it can be suppressed by piezoelectric actuators. Figure 41 and Fig. 42 depict the changes in the base's position and the angle of some arm's joints, which show that the changes with different control schemes are different.

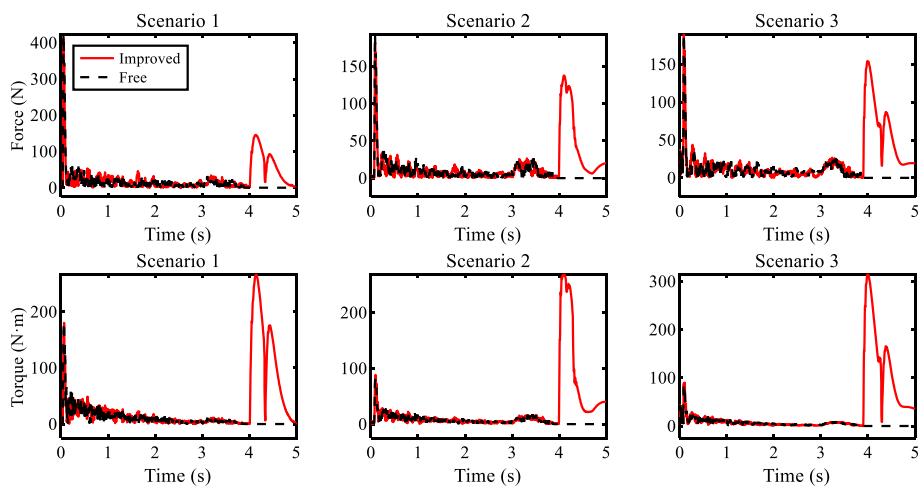


**Fig. 38** Control resultant forces and torques on the base in different scenarios

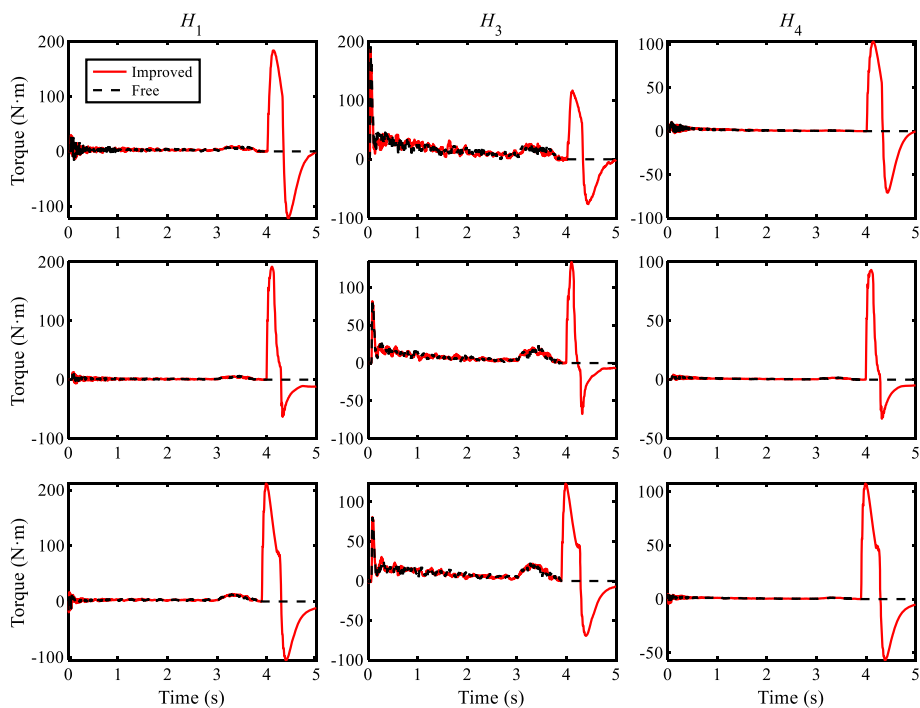


**Fig. 39** Control torques on joints in different scenarios (lines 1–3 correspond to scenarios 1–3, respectively)

## 5 Conclusion

This paper studied the control issue for a service spacecraft capturing a noncooperative spacecraft by a robotic arm. First, the capturing dynamics model was established. Accord-



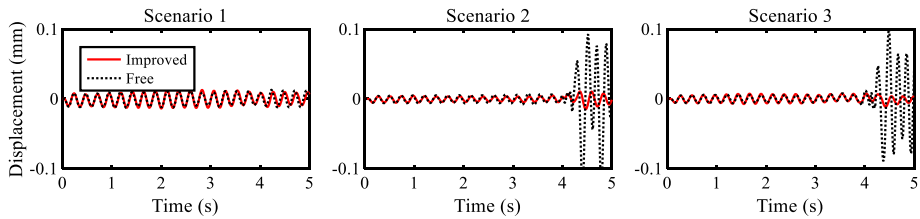


**Fig. 40** Vibration displacements in the  $y$ -direction at the endpoint of the solar panel

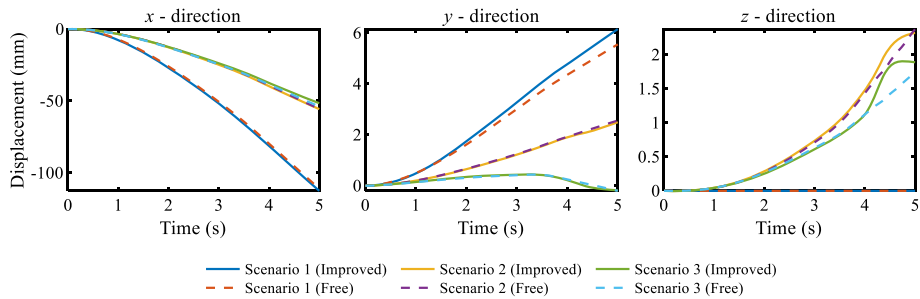


**Fig. 41** Displacement of the base in different scenarios

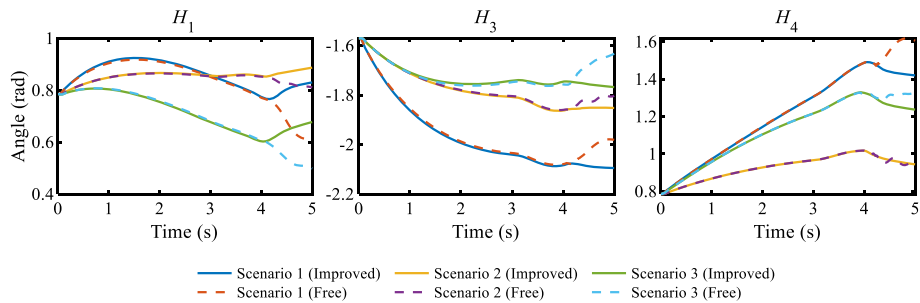


**Fig. 42** Angles of arm joints  $H_1$ ,  $H_3$ , and  $H_4$  in different scenarios

ing to the collision-scenario analysis, a new capturing strategy was proposed, dividing the capturing process into two phases: colliding and locking. The colliding phase aims to establish a stable contact between the gripper and the target surface and form a force-closure grasp configuration for the graspable structure. The locking phase aims to let the gripper lock the graspable structure and reduce the impact on the base of the service spacecraft. An improved damping-control scheme used in the collision phase was then designed to establish a stable contact, whose design concept was obtained from the study result of the “three-ball collision” problem. For the locking phase, the control scheme allows the service spacecraft to be in a free state, which is a benefit to reducing the control output. Finally, the simulation studies demonstrated the control schemes’ effectiveness and the rationality of the capture strategy. Moreover, the studies indicated the superiority of the improved control scheme to our previous control scheme, namely, the damping-control one. Future work includes phys-

ical experiments to evaluate the validity and robustness of the improved control scheme in real situations and research on choosing the optimal parameters of the controllers.

**Acknowledgements** This work was supported by the Natural Science Foundation of China (Grant Numbers: 12172214, 12172215, and 61973256)

## Declarations

**Competing Interests** The authors declare no competing interests.

## References

1. Akin, D., Sullivan, B.: A survey of serviceable spacecraft failures. In: AIAA Space 2001 Conference and Exposition, pp. 1–8. American Institute of Aeronautics and Astronautics, Reston, Virginia (2001)
2. Tafazoli, M.: A study of on-orbit spacecraft failures. *Acta Astronaut.* **64**, 195–205 (2009)
3. Shan, M., Guo, J., Gill, E.: Review and comparison of active space debris capturing and removal methods. *Prog. Aerosp. Sci.* **80**, 18–32 (2016)
4. Kaiser, C., Sjöberg, F., Delcura, J.-M., et al.: SMART-OLEV—an orbital life extension vehicle for servicing commercial spacecrafts in GEO. *Acta Astronaut.* **63**(1–4), 400–410 (2008)
5. ESA. e.Deorbit implementation plan. European Space Research and Technology Centre TEC-SC-TN-2015-007, 2015
6. Biesbroek, R., Soares, T., Husing, J.: The e.Deorbit CDF Study: A Design Study for the Safe Removal of a Large Space Debris. Proceedings of 6th European Conference on Space Debris, vol. 715, p. 12. ESA, Montreal, Canada (2013)
7. Shan, M., Guo, J., Gill, E.: An analysis of critical deployment parameters for tethered-net capturing for space debris removal. In: 66th International Astronautical Congress, Jerusalem, Israel (2015)
8. Medina, A., Cercós, L., Stefanescu, R.M., et al.: Validation results of satellite mock-up capturing experiment using nets. *Acta Astronaut.* **134**, 314–332 (2017)
9. Benvenuto, R., Lavagna, M.R.: Flexible capture devices for medium to large debris active removal: simulations results to drive experiments. In: 12th Symposium on Advanced Space Technologies in Automation and Robotics, Noordwijk, Netherlands, pp. 1–8 (2013)
10. Benvenuto, R., Pesce, V., Lavagna, M., et al.: 3D reconstruction of a space debris capturing net trajectory during microgravity experiments-results and lesson learnt. In: 67th International Astronautical Congress, Guadalajara, Mexico, pp. 1–10 (2016)
11. Forshaw, J.L., Aglietti, G.S., Navarathinam, N., et al.: RemoveDEBRIS: an in-orbit active debris removal demonstration mission. *Acta Astronaut.* **127**, 448–463 (2016)
12. Forshaw, J.L., Aglietti, G.S., Fellowes, S., et al.: The active space debris removal mission RemoveDebris. Part 1: from concept to launch. *Acta Astronaut.* **168**, 293–309 (2020)
13. Aglietti, G.S., Taylor, B., Fellowes, S., et al.: The active space debris removal mission RemoveDebris. Part 2: in orbit operations. *Acta Astronaut.* **168**, 310–322 (2020)
14. Dudziak, R., Tuttle, S., Barraclough, S.: Harpoon technology development for the active removal of space debris. *Adv. Space Res.* **56**(3), 509–527 (2015)
15. Forshaw, J., Aglietti, G., Navarathinam, N., et al.: In: An in-Orbit Active Debris Removal Mission-REMOVEDEBRIS: Pre-Launch Update 66th International Astronautical Congress, Jerusalem, Israel, pp. 1–14 (2015)
16. Forshaw, J.L., Aglietti, G.S., Salmon, T., et al.: Final payload test results for the RemoveDebris active debris removal mission. *Acta Astronaut.* **138**, 326–342 (2017)
17. Reed, J., Barraclough, S.: Development of harpoon system for capturing space debris. In: 6th European Conference on Space Debris, Darmstadt, Germany, vol. 723, p. 174 (2013)
18. Wayman, A., Ractcliffe, A., Barraclough, S., et al.: Design and testing of a full scale harpoon capture system. In: Proceedings of the 7th European Space Debris Conference, Darmstadt, Germany, vol. 7, p. 1 (2017)
19. Huang, P., Wang, D., Meng, Z., et al.: Adaptive postcapture backstepping control for tumbling tethered space robot–target combination. *J. Guid. Control Dyn.* **39**(1), 150–156 (2016)
20. Huang, P., Wang, D., Meng, Z., et al.: Impact dynamic modeling and adaptive target capturing control for tethered space robots with uncertainties. *IEEE/ASME Trans. Mechatron.* **21**(5), 2260–2271 (2016)
21. Yoshida, K., Nakanishi, H.: Impedance matching in capturing a satellite by a space robot. In: IEEE/RSSJ International Conference on Intelligent Robots and Systems (IROS), vol. 4, pp. 3059–3064 (2003)

22. Yoshida, K., Nakanishi, H., Ueno, H., Inaba, N., Nishimaki, T., Oda, M.: Dynamics, control and impedance matching for robotic capture of a non-cooperative satellite. *Adv. Robot.* **18**(2), 175–198 (2004)
23. Nakanishi, H., Yoshida, K.: Impedance control for free-flying space robots-basic equations and applications. In: *IEEE/RSJ International Conference on Intelligent Robots and Systems (IROS)*, pp. 3137–3142 (2006)
24. Uyama, N., Hirano, D., Nakanishi, H., Nagaoka, K., Kazuya, Y.: Impedance-based contact control of a free-flying space robot with respect to coefficient of restitution. In: *IEEE/SICE International Symposium on System Integration (SII)*, pp. 1196–1201 (2011)
25. Uyama, N., Nakanishi, H., Nagaoka, K., Yoshida, K.: Impedance-based contact control of a free-flying space robot with a compliant wrist for non-cooperative satellite capture. In: *IEEE/RSJ International Conference on Intelligent Robots and Systems (IROS)*, pp. 4477–4482 (2012)
26. Ma, G., Jiang, Z., Li, H., Gao, J., Yu, Z. et al.: Hand-eye servo and impedance control for manipulator arm to capture target satellite safely. *Robotica* **33**(4), 848–864 (2015)
27. Flores-Abad, A., Zhang, L., Wei, Z., Ma, O.: Optimal capture of a tumbling object in orbit using a space manipulator. *J. Intell. Robot. Syst.* **86**(2), 199–211 (2017)
28. Mou, F., Wu, S., Xiao, X., Zhang, T., Ma, O.: Control of a space manipulator capturing a rotating object in the three-dimensional space. In: *International Conference on Ubiquitous Robots*, pp. 763–768 (2018)
29. Wu, S., Mou, F., Liu, Q., Cheng, J.: Contact dynamics and control of a space robot capturing a tumbling object. *Acta Astronaut.* **151**, 532–542 (2018)
30. Liu, X.-F., Cai, G.-P., Wang, M.-M., Chen, W.-J.: Contact control for grasping a non-cooperative satellite by a space robot. *Multibody Syst. Dyn.* **50**(2), 119–141 (2020)
31. Liu, X.F., Zhang, X.Y., Chen, P.C., Cai, G.P.: Hybrid control scheme for grasping a non-cooperative tumbling satellite. *IEEE Access* **8**, 54963–54978 (2020)
32. Stolfi, A., Gasbarri, P., Sabatini, M.: A combined impedance-PD approach for controlling a dual-arm space manipulator in the capture of a non-cooperative target. *Acta Astronaut.* **139**, 243–253 (2017)
33. Stolfi, A., Gasbarri, P., Sabatini, M.: A parametric analysis of a controlled deployable space manipulator for capturing a non-cooperative flexible satellite. *Acta Astronaut.* **148**, 317–326 (2018)
34. Dai, H., Cao, X., Jing, X., Wang, X., Yue, X.: Bio-inspired anti-impact manipulator for capturing non-cooperative spacecraft: theory and experiment. *Mech. Syst. Signal Process.* **142**, 106785 (2020)
35. Liu, X.-F., Li, H.-Q., Wang, J.-S.: Dynamics analysis of flexible space robot with joint friction. *Aerosp. Sci. Technol.* **47**, 164–176 (2015)
36. Lankarani, H.M., Nikravesh, P.E.: A contact force model with hysteresis damping for impact analysis of multibody systems. *J. Mech. Des. Trans. ASME* **112**, 369–376 (1990)
37. Banerjee, A., Chanda, A., Das, R.: Historical origin and recent development on normal directional impact models for rigid body contact simulation: a critical review. *Arch. Comput. Methods Eng.* **24**, 397–422 (2017)
38. Carvalho, A.S., Martins, J.M.: Exact restitution and generalizations for the Hunt–Crossley contact model. *Mech. Mach. Theory* **139**, 174–194 (2019)
39. Safaeifar, H., Farshidianfar, A.: A new model of the contact force for the collision between two solid bodies. *Multibody Syst. Dyn.* **50**, 233–257 (2020)
40. Ma, J., Qian, L., Chen, G., Li, M.: Dynamic analysis of mechanical systems with planar revolute joints with clearance. *Mech. Mach. Theory* **94**, 148–164 (2015)
41. Zhang, J., Li, W., Zhao, L., He, G.: A continuous contact force model for impact analysis in multibody dynamics. *Mech. Mach. Theory* **153**(1), 103946 (2020)
42. Moosavian, S.A.A., Papadopoulos, E.: Free-flying robots in space: an overview of dynamics modeling, planning and control. *Robotica* **25**, 537–547 (2007)

**Publisher's Note** Springer Nature remains neutral with regard to jurisdictional claims in published maps and institutional affiliations.

Springer Nature or its licensor (e.g. a society or other partner) holds exclusive rights to this article under a publishing agreement with the author(s) or other rightsholder(s); author self-archiving of the accepted manuscript version of this article is solely governed by the terms of such publishing agreement and applicable law.